Discrete Element and Experimental Investigations of the Earth Pressure Distribution on Cylindrical Shafts

Viet D. H. Tran[1]; Mohamed A. Meguid[2]; and Luc E. Chouinard, M.ASCE[3]

Abstract: Experimental and numerical studies have been conducted to investigate the earth pressure distribution on cylindrical shafts in soft ground. A small-scale laboratory setup that involves a mechanically adjustable lining installed in granular material under an axisymmetric condition is first described. The earth pressure acting on the shaft and the surface displacements are measured for different induced wall movements. Numerical modeling is then performed using the discrete element method to allow for the simulation of a large soil displacement and particle rearrangement near the shaft wall. The experimental and numerical results are summarized and compared against previously published theoretical solutions. The shaft-soil interaction is discussed, and conclusions regarding soil failure and the earth pressure distributions in both the radial and circumferential directions are presented. **DOI: 10.1061/(ASCE)GM.1943-5622.0000277.**

Author keywords: Cylindrical shafts; Soil arching; Lateral earth pressure; Retaining structures; Discrete element method.

Introduction

The discrete element method (DEM) has gained popularity in the past few decades among geotechnical engineers and researchers involved in studying soil-structure interaction problems. Since it was first proposed by Cundall and Strack (1979), the method has been used extensively to understand the micromechanical and macromechanical behavior of granular material (e.g., Jiang et al. 2003; Cui and O'Sullivan 2006; Yan and Ji 2010; Chen et al. 2012). One approach to implement DEM into geotechnical engineering analysis is by fitting the measured macroscale response for a given problem with that predicted using the DEM method. Although extensive research has been reported on quantitative DEM validation using standardized laboratory tests, such as direct shear and triaxial experiments (Liu et al. 2005; Cui and O'Sullivan 2006; Belheine et al. 2009; O'Sullivan and Cui 2009), DEM validation conducted using large-scale problems (Jenck et al. 2009; Chen et al. 2012) is considered to be limited.

This study aims at providing a quantitative DEM validation of a practical geotechnical problem involving a buried structure interacting with the surrounding soil. The active earth pressure distribution on cylindrical shafts is selected because it involves large displacements and particle movements under an axisymmetric condition. This problem has received extensive research attention in an effort to understand the mechanics behind the observed lateral earth pressure distribution along vertical shafts using experimental and theoretical investigations. Among the reported experimental studies that involved measuring lateral earth pressure due to the movement of a shaft wall are those of Walz (1973); Lade et al. (1981); Konig et al. (1991); Chun and Shin (2006); and Tobar and Meguid (2011). Theoretical solutions have also been proposed by researchers to calculate lateral earth pressures on cylindrical structures, taking into account the interaction between the cylindrical wall and the surrounding material (e.g., Cheng and Hu 2005; Cheng et al. 2007; Salgado and Prezzi 2007; Andresen et al. 2011; Osman and Randolph 2012).

An attempt has been made by Herten and Pulsfort (1999) to use the DEM to simulate a laboratory size shaft construction in granular material. Although the study provided useful results, the circular shaft was assumed to behave as a small flat wall, which has lead to an inadequate simulation of the arching effect and the stress distribution around the shaft. Furthermore, a quite small segment of the shaft geometry was modeled, resulting in the presence of rigid boundaries close to the investigated area. Therefore, there is a need for an improved DEM simulation of the problem, considering the problem geometry as well as realistic soil properties.

In this paper, an experimental study of a model shaft installed in granular material is first presented. The recorded lateral earth pressures acting on the shaft with different wall movements is measured. A DEM model that has been developed to simulate the shaft model is then introduced. A suitable packing method to generate the soil domain is proposed, and a calibration test is conducted to determine the input parameters needed for the simulation. The results of the experimental and numerical studies are then analyzed, and conclusions are made regarding the distribution of the radial and circumferential stresses around the shaft as well as the extent of soil shear failure.

Experimental Study

An experimental study was performed to investigate the active earth pressure on circular shafts in dry sand. During the experiment, the shaft diameter was uniformly reduced while the radial earth pressures at different depths were recorded. The experimental setup

[1]Graduate Student, Dept. of Civil Engineering and Applied Mechanics, McGill Univ., 817 Sherbrooke St. West, Montreal, QC, Canada H3A 2K6. E-mail: viet.tran@mail.mcgill.ca

[2]Associate Professor, Dept. of Civil Engineering and Applied Mechanics, McGill Univ., 817 Sherbrooke St. West, Montreal, QC, Canada H3A 2K6 (corresponding author). E-mail: mohamed.meguid@mcgill.ca

[3]Associate Professor, Dept. of Civil Engineering and Applied Mechanics, McGill Univ., 817 Sherbrooke St. West, Montreal, QC, Canada H3A 2K6. E-mail: luc.chouinard@mcgill.ca

Note. This manuscript was submitted on June 2, 2012; approved on December 4, 2012; published online on December 6, 2012. Discussion period open until July 1, 2014; separate discussions must be submitted for individual papers. This paper is part of the ***International Journal of Geomechanics***, Vol. 14, No. 1, February 1, 2014. ©ASCE, ISSN 1532-3641/2014/1-80–91/$25.00.

Int. J. Geomech. 2014.14:80-91.

consisted of an instrumented shaft installed in soil contained within a cylindrical concrete tank. Details of the test setup and procedure have been reported elsewhere (Tobar and Meguid 2011) and are briefly summarized subsequently.

Model Shaft

The model shaft consisted of six curved lining segments cut from a steel tube with an outer diameter of 101.6 mm and a thickness of 6.35 mm. The lining segments were fixed in segment holders, which in turn were attached to hexagonal nuts using steel hinges (see Fig. 1). The nuts could move vertically along an axial rod that could be rotated using a precalibrated handle. The shaft was placed on a Plexiglas plate attached firmly to the base of the container. The initial diameter of the shaft is 150 mm, and the length of the shaft is 1,025 mm, with a surrounding soil height of 1,000 mm. Shims bent from gauge steel strips were used to cover the spaces between the lining segments. They were placed on the outer surface of the lining and overlapped the steel segments such that one edge of each shim was fixed to one lining segment, whereas the other edge was free to slide over the lining segment. This mechanism keeps the shaft segments from colliding into one another during the inward movement and at the same time assures a gap-free circumference reduction process [Fig. 1(c)].

To reduce the shaft diameter, the axial rod is rotated, forcing the hexagonal nuts to move vertically; the segment holders and the lining segments are then pulled radially inward. These movements force the shaft diameter to decrease uniformly. Two additional segment guide disks were also installed [Fig. 1(b)] to protect the shaft linings from rotational movement or sliding out of the segment holders.

Concrete Container

A cylindrical concrete tank with an inner diameter of 1,220 mm provided the axisymmetric condition for the experiment. The tank diameter was chosen to minimize the boundary effects on the behavior of the soil-shaft interaction during the experiment. Previous experimental results of Chun and Shin (2006) and Prater (1977) suggest that the soil failure zone extends laterally from one to three times the shaft radius. Therefore, negligible soil movement is expected in the present investigation at a radial distance of 240 mm from the outer perimeter of the shaft lining. The depth of the container is 1,070 mm to support the full length of the shaft. The interior side of the container was smoothed and lined with plastic sheets to reduce the soil-wall friction. In addition, a sand auger system was used to remove the sand after each test through a circular hole 150 mm in diameter located sideways at the base of the container. Fig. 1(a) shows an overview of the experimental setup and model shaft.

Data Recording

Load cells and displacement transducers were used to measure earth pressure and wall movement during the test. Three load cells were installed behind the lining segments at three locations along the shaft: 840, 490, and 240 mm below the sand surface, respectively. The load cells were equipped with sensitive circular areas of 1-in. diameter in contact with the soil. Two displacement transducers were located near the top and bottom of the shaft lining. All load cells and displacement transducers were connected to a data acquisition system and controlled though a personal computer.

Testing Procedure

Before each test, all instruments were examined and the shaft was adjusted to have an initial diameter of 150 mm. The concrete container was then filled with coarse sand (Granusil silica 2075, Unimin Corporation, St.-Adrien, Quebec, Canada) through a raining process with a target depth of 1 m from the shaft base. Table 1 summarizes the sand properties. A hopper positioned 1,500 mm above the tank

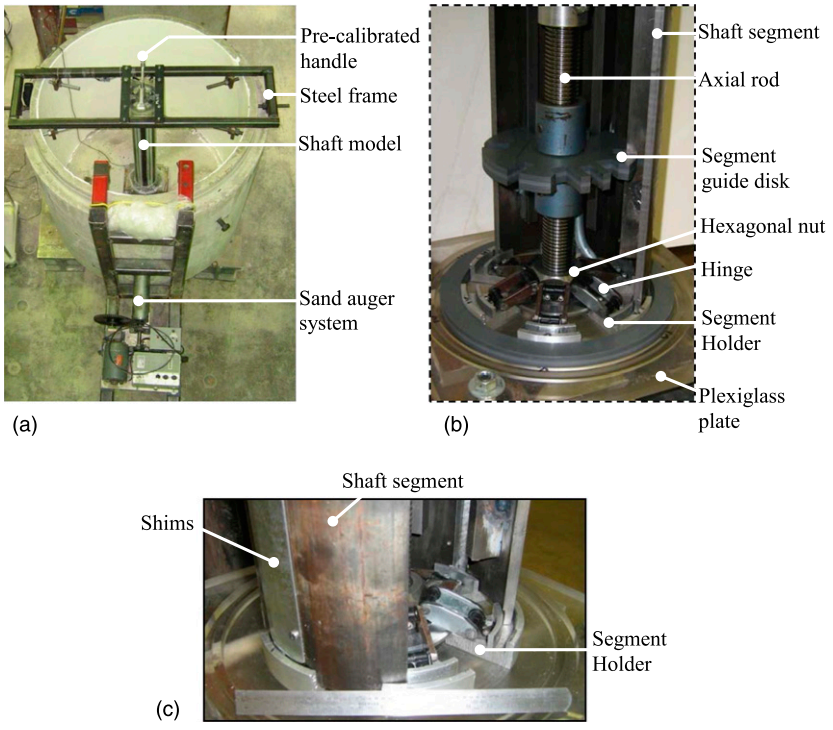

Fig. 1. (a) Overview of the experimental setup; (b) model shaft during assemblage; (c) lower-end section during assemblage (Tobar 2009; with permission)

Int. J. Geomech. 2014.14:80-91.

Table 1. Soil Properties Used in the Experimental Study

Parameter	Value
Specific gravity	2.65
Coefficient of uniformity (C_u)	3.6
Coefficient of curvature (C_c)	0.82
Void ratio	0.78
Unit weight (kN/m^3)	14.7
Internal friction angle ϕ (degrees)	41
Cohesion (kN/m^2)	0

was used to spread the sand uniformly over the container. Sand was placed in three layers, and as soon as the sand height reached slightly over 1 m, the raining process was stopped and extra sand was removed. The sand height was checked using laser sensors to ensure consistent initial conditions for each test. The shaft diameter was then reduced slowly, and readings were taken for each movement increment. The test was stopped when the reduction in the shaft radius reached 5 mm. Selected experimental results are discussed in the "Results and Discussion."

Discrete Element Simulation

The DEM considers the interaction among distinct particles at their contact points. Different types of particles have been developed, including discs, spheres, ellipsoids, and clumps. Particles in a sample may have variable sizes to represent the grain size distribution of the real soil. The interaction among particles is regarded as a dynamic process that reaches static equilibrium when the internal and external forces are balanced. The dynamic behavior is represented by a time-step algorithm using an explicit time-difference scheme. Newton's and Euler's equations are then used to determine particle displacement and rotation. The DEM simulations in this study are conducted using the open source discrete element code YADE (Kozicki and Donze 2009; Šmilauer et al. 2010). Spherical particles of different sizes are used to represent sand particles throughout the numerical investigation. The contact law among particles is briefly described subsequently.

If two particles A and B with radii r_A and r_B are in contact, the contact penetration depth is defined as

$$\boldsymbol{\Delta} = r_A + r_B - d_0 \tag{1}$$

where d_0 = distance between the two centers of particles A and B.

The force vector $\mathbf{F}$, which represents the interaction between the two particles, is decomposed into normal and tangential forces

$$\mathbf{F}_N = K_N \cdot \boldsymbol{\Delta}_N, \quad \delta\mathbf{F}_T = -K_T \cdot \delta\boldsymbol{\Delta}_T \tag{2}$$

where $\mathbf{F}_N$ and $\mathbf{F}_T$ = normal and tangential forces; K_N and K_T = normal and tangential stiffnesses at the contact; $\delta\boldsymbol{\Delta}_T$ = incremental tangential displacement; $\delta\mathbf{F}_T$ = incremental tangential force; and $\boldsymbol{\Delta}_N$ = normal penetration between the two particles. The stiffnesses K_N and K_T are defined by

$$K_N = \frac{k_n^{(A)} k_n^{(B)}}{k_n^{(A)} + k_n^{(B)}} \tag{3}$$

where $k_n^{(A)}$ and $k_n^{(B)}$ = particle normal stiffnesses.

The particle normal stiffness is related to the particle material modulus E and particle diameter $2r$ such that

$$k_n^{(A)} = 2E_A r_A, \quad k_n^{(B)} = 2E_B r_B \tag{4}$$

The stiffness K_N can be rewritten as

$$K_N = \frac{2E_A r_A E_B r_B}{E_A r_A + E_B r_B} \tag{5}$$

The interaction tangential stiffness K_T is determined as a given fraction of the computed K_N. The macroscopic Poisson's ratio is determined by the K_T/K_N ratio, while the macroscopic Young's modulus is proportional to K_N and affected by K_T/K_N. The tangential force $\mathbf{F}_T$ is limited by a threshold value such that

$$\mathbf{F}_T = \frac{\mathbf{F}_T}{\|\mathbf{F}_T\|}\|\mathbf{F}_N\|\tan(\varphi_{\text{micro}}) \quad \text{if } \|\mathbf{F}_T\| \geq \|\mathbf{F}_N\|\tan(\varphi_{\text{micro}}) \tag{6}$$

where φ_{micro} = microscopic friction angle.

To represent the rolling behavior between two particles A and B, a rolling angular vector $\boldsymbol{\theta}_r$ is used. This vector describes the relative orientation change between the two particles and can be defined by summing the angular vector of the incremental rolling (Belheine et al. 2009; Šmilauer et al. 2010)

$$\boldsymbol{\theta}_r = \sum d\boldsymbol{\theta}_r \tag{7}$$

A resistant moment $\mathbf{M}_r$ is computed by

$$\mathbf{M}_r = \begin{cases} K_r\boldsymbol{\theta}_r & \text{if } K_r\|\boldsymbol{\theta}_r\| < \|\mathbf{M}_r\|_{\lim} \\ \|\mathbf{M}_r\|_{\lim}\frac{\boldsymbol{\theta}_r}{\|\boldsymbol{\theta}_r\|} & \text{if } K_r\|\boldsymbol{\theta}_r\| \geq \|\mathbf{M}_r\|_{\lim} \end{cases} \tag{8}$$

where

$$\|\mathbf{M}_r\|_{\lim} = \eta_r\|\mathbf{F}_N\|\frac{r_A + r_B}{2} \tag{9}$$

The variable K_r is the rolling stiffness of the interaction computed by

$$K_r = \beta_r\left(\frac{r_A + r_B}{2}\right)^2 K_T \tag{10}$$

where β_r = rolling resistance coefficient; and η_r = dimensionless coefficient.

To record macroscopic stress components, a measurement rectangular box with volume V is used. The average stresses within the box are given by

$$\sigma_{ij} = \frac{1}{V}\sum_{c=1}^{N_c} x^{c,i} f^{c,j} \tag{11}$$

where N_c = number of contacts within the measurement box; $f^{c,j}$ = contact force vector at contact c; $x^{c,i}$ = branch vector connecting two contact particles A and B; and indexes i and j indicate the Cartesian coordinates.

DEM Sample Generation

In this study, an appropriate sample generation technique is proposed to generate DEM samples for both the calibration test and shaft simulation. Although there are several available methods that can be used to construct DEM specimens, no agreement has been reached regarding the most suitable approach to generate soil specimens. Users have to adopt methods that provide the best replication of the real packing process while keeping the computational

Int. J. Geomech. 2014.14:80-91.

cost acceptable. Because the sand used in the physical test was generated in layers under gravity, the gravitational approach appears to be a suitable choice in the current study. Although other techniques, such as the compression method (Cundall and Strack 1979), triangulation-based approach (Labra and Oñate 2009), and radius expansion method (Itasca 2004), can minimize the time required to generate specimens, they have certain features that are not suitable for this study. For example, the compression method uses pressurized boundaries to maintain the equilibrium condition, which violates the initial condition in a real sand deposit, whereas the triangulation-based approach lacks the control of the particle size distribution, which is necessary to replicate real soil behavior. The radius expansion approach tends to generate a specimen with an isotropic stress state (O'Sullivan 2011).

The gravitational packing technique used in this study is a multilayer packing method. This packing technique originated from the one proposed by Ladd (1978) for real specimen preparation and is similar to the multilayer with undercompaction method proposed by Jiang et al. (2003). Modifications are made to simulate the real packing of the sand around the vertical shaft. The packing procedure is described as follows.

The number of layers is first chosen, and the volume of particles for each layer is calculated based on the target void ratio of the final soil specimen. Fig. 2 illustrates the packing procedure. To generate the first layer, a set of noncontacting particles is first generated inside a box following a predetermined particle size distribution until the target volume is reached. The height of the box is chosen to be larger than the target height of the layer to insure that all particles can be generated without overlapping. Gravity is then applied to all particles, allowing them to move downward and come in contact with each other. The interparticle friction angle is set to 0. It is noticed that even when the friction angle is 0, the DEM-generated samples are generally looser than the real ones. Cui and O'Sullivan (2006) made the same observation. To increase the density of the packing, a lateral shaking movement is applied to the box to help small particles move into voids between larger particles. The first layer generation is completed when the system reaches equilibrium. For the second layer, the height of the box is increased and the second cloud of noncontacting particles is generated in the area above the existing particles. Gravity and shaking are then applied, and the system is allowed to come into equilibrium. The procedure is repeated until the final specimen is formed. The proposed multilayer approach helps increase the density of the packing while keeping the packing pattern realistic. A packing process of approximately 200,000 particles using 10 packing layers requires nearly 48 running hours on a personal computer to reach equilibrium that is considered acceptable with respect to DEM simulations.

The behavior of a DEM specimen depends not only on the packing structure but also on the particle size distribution. It is essential that particle generation follows the predefined particle size distribution that has a great influence on the behavior of the discrete element system. However, the true replication of grain size is usually restricted by the high computational cost caused by the large number of particles. Because the volume of a particle with radius r is proportional to r^3, a large number of small particles is needed to generate a very small volume. This leads to an extremely high number of particles required to fill up the soil domain that in turn dramatically increases the simulation cost. In addition, the high computational cost is also caused by the decrease in the critical time step needed for stable analysis that is proportional to the mass of the particles. For these reasons, particles smaller than a particle diameter corresponding to 5% passing, D_5, are neglected in this study to reduce the computational cost. This is appropriate because these particles are assumed to have a minor effect on the force chains that transmit stresses within the sample (Cheung 2010; Calvetti 2008).

For the simulation of large-scale problems, particle upscaling is often used to reduce the number of modeled particles. Careful consideration of particle sizes is usually made to keep balance between the computational cost and the scaling effects on the sample responses. In this study, the scale factors (ratio of a numerical particle size to its real particle size) are chosen as 4 and 25 for the direct shear test and the large scale shaft simulation, respectively, and will be discussed in the following sections. Fig. 3 shows the particle size distributions used in the DEM analysis in simulating the direct shear tests and the shaft model.

Model Calibration Using Direct Shear Test

To determine the input parameters for the numerical model, calibration is first conducted using the results of the direct shear tests. Numerical simulations of direct shear tests are performed, and microscopic parameters for the DEM simulation are identified by comparing the numerical results with the experimental data.

The apparatus used for the physical tests consists of a shear box (60×60 mm) split horizontally into two halves. To apply direct shear to the sample, one part of the box was moved with a constant

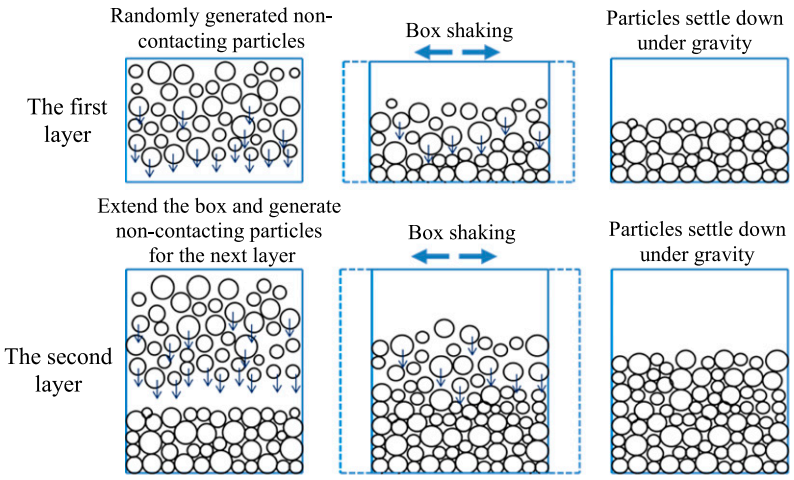

Fig. 2. Multilayer gravitational packing procedure

Int. J. Geomech. 2014.14:80-91.

velocity of 0.021 mm/s, while the other part was kept stationary. Three different normal stresses (13.6, 27.3, and 40.9 kPa) were applied using vertical loads on top of the shear box. The initial sample height was approximately 25 mm, with a height-to-width ratio of 1:2.4.

The numerically simulated shear box consists of two parts, and each part comprises five rigid boundaries: one horizontal and four vertical boundaries [Fig. 4(a)]. The numerical shear box has the same dimensions as the actual one to replicate the testing conditions. A specimen is generated using the gravitational method described in the previous section. Because the size of the box is relatively small, only one packing layer is necessary, and all particles are generated and settled at the same time. Using a scale factor of 4, the generated specimen consists of over 14,000 particles with diameters ranging from 1.0 to 4.0 mm. This number of used particles is considered sufficient to represent the test and consistent with that used in previous studies (Cui and O'Sullivan 2006; Yan and Ji 2010).

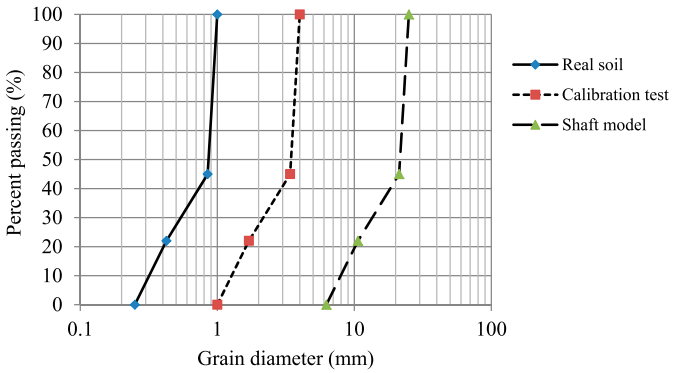

Fig. 3. Grain size distributions

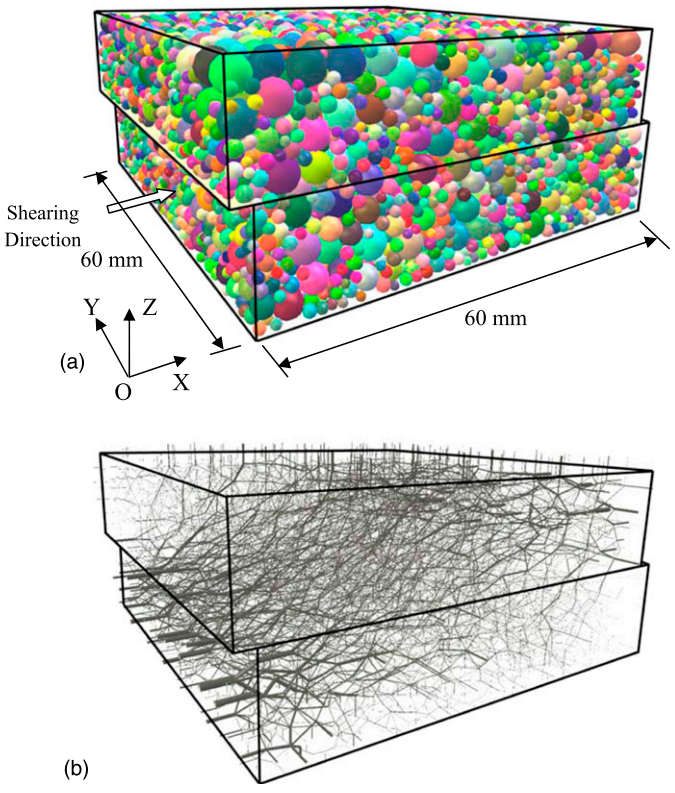

Fig. 4. (a) Three-dimensional direct shear sample; (b) contact force network at a shear displacement of 2 m

After the sample generation is completed, the specimen is subjected to three different vertical stresses of 13.6, 27.3, and 40.9 kPa. During shearing, one part of the shear box is moved with a displacement rate consistent with that used in the actual test, allowing the upper boundary to freely move in the vertical direction. When the current normal stress (σ) does not match the desired value (σ_0), the upper plate is adjusted by moving it in the vertical direction at a distance of $dy = (\sigma - \sigma_0)/K$, where the stiffness K is determined by adding the stiffnesses of all active particle–upper plate interactions. This method allows for the normal stress to be maintained with an error of less than 1%.

Model calibration is generally a challenging task because the behavior of the discrete element samples depends not only on the microscopic parameters, but also on particle shapes, particle size distribution, contact models, and the packing technique. While the adopted packing method and particle size distribution are considered realistic, spherical particle shapes and the contact model are somewhat artificial. These assumptions are usually overcome by choosing appropriate input parameters for the simulation. Other researchers have successfully used this calibration approach (Belheine et al. 2009).

The most important microscopic parameters that would affect the behavior of the direct shear test are the friction angle, rolling resistance, and contact stiffnesses. These parameters are varied to match the results obtained from the real test data. Other parameters are identified as follows: particle density is 2,650 kg/m^3 following the specific gravity of the sand, particle cohesion is set to 0, and the K_T/K_N ratio is fixed to be 0.25, as suggested by Calvetti (2008). It is noted that the friction angle between particles and the upper and lower walls of the box is given a value of 45° to reduce the slippage at these boundaries. Frictionless contacts at all vertical plates are assumed.

To perform the calibration, the shear displacement–shear stress curves are plotted for the three applied normal stresses. The shear stress is calculated as the sum of forces in the x-direction acting on the upper boundary divided by the cross-sectional area, and the normal stress is calculated as the total force acting on the upper plate divided by the cross-sectional area. The rolling resistance coefficient (β_R) together with the normal and tangential stiffnesses are varied first to match the slope of the curve; the friction angle is then modified to match the peak shear stress. It is observed that the most appropriate combination is a friction angle of 34°, β_R of 0.05, and particle material modulus of 38 MPa. Table 2 summarizes the selected parameters. Fig. 5 presents the results of the discrete element analysis along with the experimental data. To illustrate the changes in contact forces during the test, Fig. 4(b) illustrates the force network among particles for an applied lateral displacement of 2 mm. The centers of contacting particles are connected using lines, with thickness representing the magnitude of the normal contact force. The figure shows that contact forces are transmitted diagonally from the lower left side to the upper right side of the box. Other authors

Table 2. Particles' Properties for DEM Simulations

Parameter	Value
Particle density (kg/m^3)	2,650
Particle material modulus E (MPa)	38
Ratio K_T/K_N	0.25
Friction angle ϕ (degrees)	34
β_R	0.05
η_R	1
Damping coefficient	0.2

Int. J. Geomech. 2014.14:80-91.

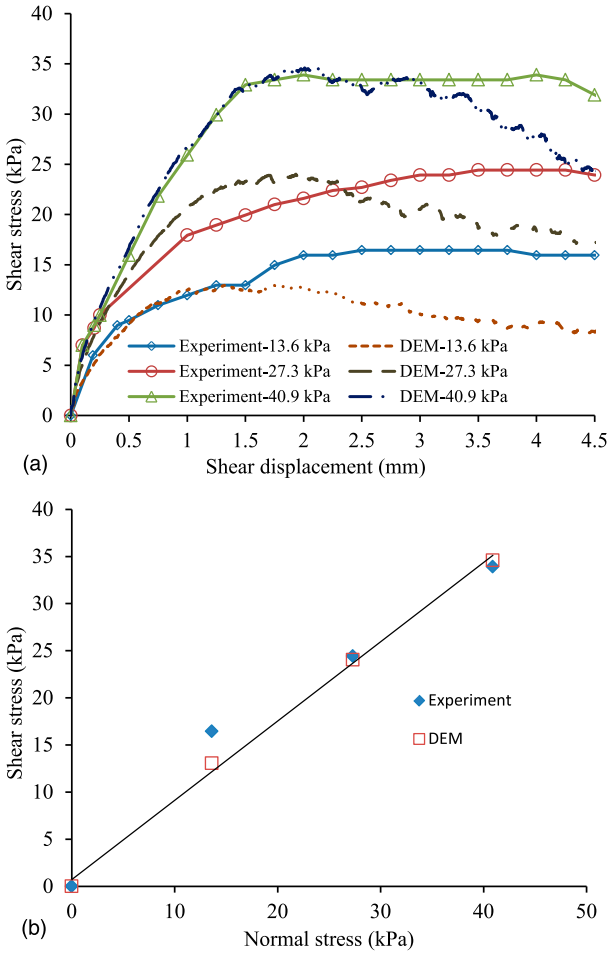

Fig. 5. Direct shear test results

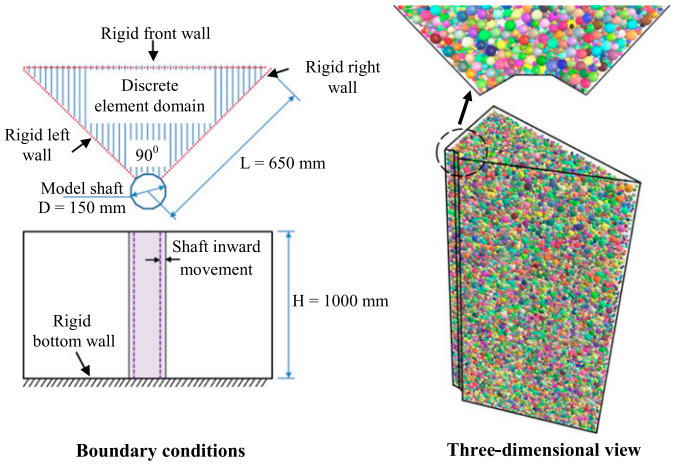

Fig. 6. Boundary conditions and three-dimensional views of the model shaft

(Yan and Ji 2010; Thornton and Zhang 2003) have observed this anisotropic force distribution.

Shaft-Soil Interaction

The vertical shaft is modeled using a cylinder 1.0 m in height and an initial diameter of 150 mm that comprises 12 equally distributed segments. Because the modeled problem is axisymmetric, only part of the domain is analyzed to reduce the computational cost. In addition, a better representation of the experiment can be achieved by simulating one slice of the soil domain with a large number of particles while keeping the simulation time acceptable. To capture the axisymmetric geometry, the model consists of a quarter of the cylindrical shaft with four boundaries, including three vertical and one horizontal boundary representing the base of the container (Fig. 6). The modeled section of the shaft is divided into three segments to capture the curved shaft geometry. The friction angle between the particles and wall boundaries is set to 0, and the earth pressures acting on the shaft are recorded within the middle of the height to reduce the boundary effects. Weatherley et al. (2011) used a similar technique in modeling a hopper flow problem.

The soil domain is generated using the proposed multilayer packing technique with a total of 10 layers. To replicate the actual soil generation process, the frictional coefficient between the particles and shaft is assigned a value of 0.2 to account for the frictional contact between the shaft and the soil. This frictional condition is maintained throughout the numerical simulation process. Using a scale factor of 25, a total of over 245,000 particles are generated with diameters ranging from 6.25 to 25 mm. The average void ratio of the generated soil sample is approximately 0.85, which is slightly greater than the void ratio of the real sand (0.78). This is attributed in part to the removal of excess sand during sample generation to reach the target height.

The generated discrete element sample is checked to ensure that it has the same characteristics as the specimen used in the direct shear test. The fabric tensor and coordination number are determined for the two samples at their initial states. The fabric tensor is given by

$$\mathbf{\Phi}_{ij} = \frac{1}{N_c} \sum_{N_c} n_i n_j \tag{12}$$

where N_c = number of contacts; and n_i = unit branch vector component in the i direction.

The coordination number N is defined as

$$N = \frac{2N_c}{N_p} \tag{13}$$

where N_p = number of particles.

Both specimens have almost the same coordination number of approximately 6.3, and the fabric tensor components are also nearly identical ($\mathbf{\Phi}_{xx}$ and $\mathbf{\Phi}_{yy}$ of approximately 0.33 and $\mathbf{\Phi}_{zz}$ of approximately 0.34, where z is the gravitational direction), which confirms the equivalence of the two soil samples.

The input parameters are then assigned to the discrete element particles based on the results of the calibration test. The scale factors used in the validation process and in modeling the shaft were examined to ensure that the microscopic parameters obtained can be used in simulating the shaft. Model validation using the direct shear test provided two important microscopic parameters: the particle stiffnesses and friction angle. Preliminary analyses indicated that stiffnesses have a very small effect on the overall response; only the particle friction angle was considered in determining the scale factor for the model validation. Different scale factors were tested to examine the variability of the macrofriction angle with the change in particle size. It is found that for scale factors of 2, 3, 4, and 5, the macroscopic friction angle varies in a narrow range between 38 and 41.5°. The randomness of the generation process at these scale factors has a minor effect on the macroresponse because the number

Int. J. Geomech. 2014.14:80-91.

of particles of the specimen has become large enough to represent the sample. Larger scale factors lead to a wide scattering of the macrofriction angle due to the decrease of the number of particles (less than 8,000 particles). The microscopic parameters were obtained from the direct shear model using a scale factor of 4; therefore, it can reasonably represent the actual granular material. According to Potyondy and Cundall (2004), when the number of particles is large enough (in the shaft, simulation is over 245,000 particles with a scale factor of 25), the macroscopic response becomes independent of the particle sizes. Therefore, the microscopic parameters of the validation can be used for the shaft simulation.

The diameter of the shaft is incrementally reduced to capture the active condition. Lateral earth pressures on the shaft and stresses in the soil domain are numerically recorded at different wall movements using Eq. (11). Stresses are obtained using measurement boxes with dimensions of $0.08 \times 0.08 \times 0.08$ m. The simulation process is considered complete when reduction in the shaft radius reaches 5 mm.

Results and Discussion

Selected experimental results (Tests T5, T6, and T7) are reported in this section at three different locations. The measured earth pressure is then compared with that calculated using the DEM analysis. Fig. 7 shows the calculated and measured initial earth pressures on the cylindrical shaft wall along with the conventional at-rest condition (K_o line where $K_o = 1 - \sin\phi$). The figure shows that the DEM results are consistent with the measured earth pressure values.

Earth Pressure Reduction with Wall Movement

Figs. 8–11 show the lateral pressures at different locations along the shaft. Pressures are plotted in these figures versus wall movements. Both the DEM simulation and the experimental results showed a consistent reduction in lateral pressures as the wall movement increases. The earth pressure became independent of the wall movement when the displacement reached approximately 3 mm. To study the effects of the wall movement on the active earth pressure, the pressure, p, at a given depth is normalized with respect to the initial value, p_0. Figs. 12–14 illustrate the normalized earth pressures at the three examined levels (0.24, 0.49, and 0.84H) for different shaft wall movements, respectively. It can be seen that the DEM results are in good agreement with the experimental data. For a very small wall movement, a large reduction in lateral earth pressure is observed. For example, at a wall movement of 0.5 mm, the calculated earth pressures decreased from 100 to 55% at 0.24 and 0.49H and to 45% at 0.84H.

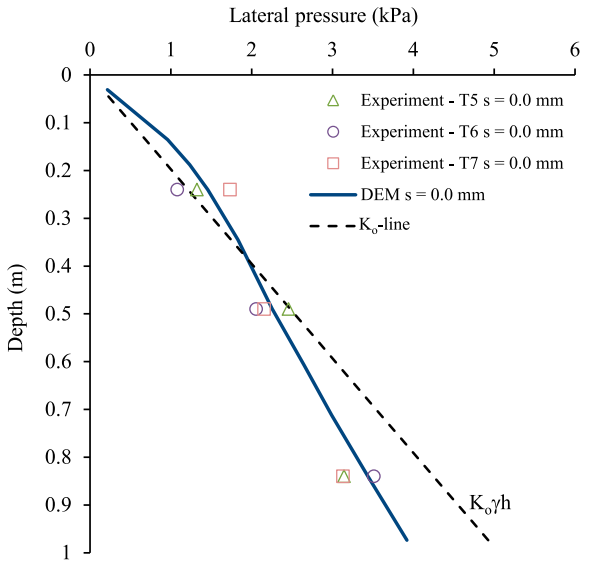

Fig. 7. Initial earth pressures on the shaft

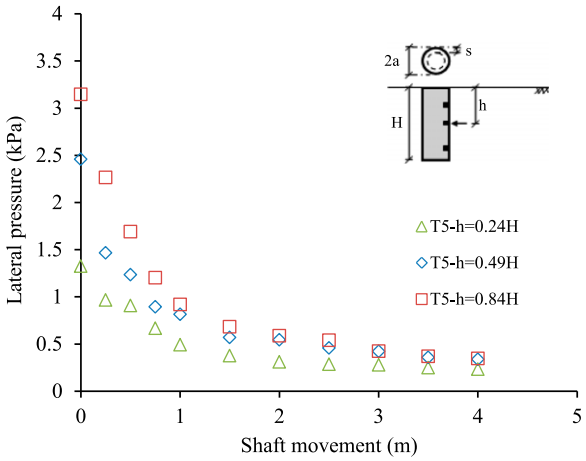

Fig. 8. Earth pressures on the shaft at different depths: Test T5

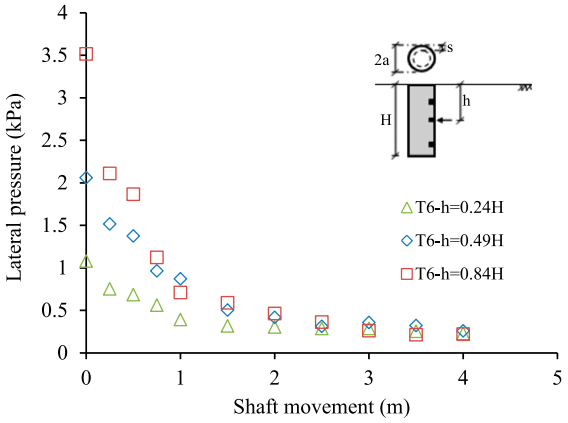

Fig. 9. Earth pressures on the shaft at different depths: Test T6

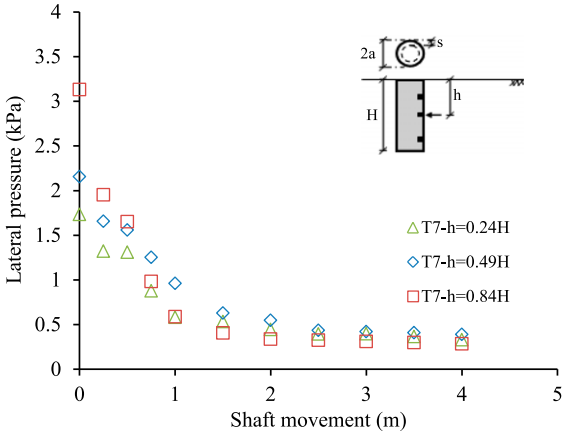

Fig. 10. Earth pressures on the shaft at different depths: Test T7

Int. J. Geomech. 2014.14:80-91.

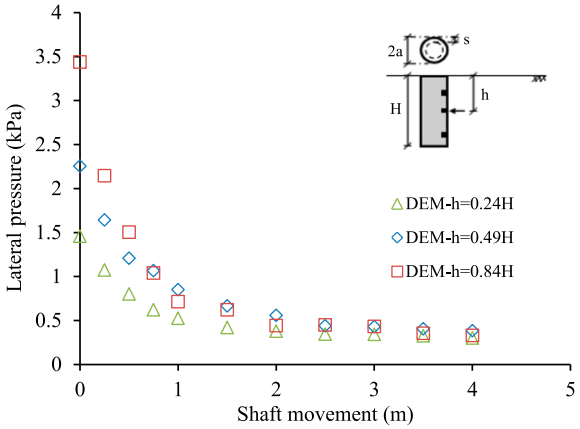

Fig. 11. Earth pressures on the shaft at different depths: DEM simulation

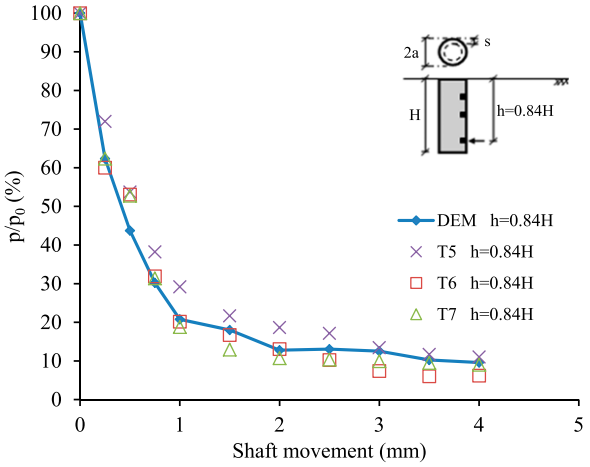

Fig. 14. Normalized pressures on the shaft at a depth of 0.84*H*

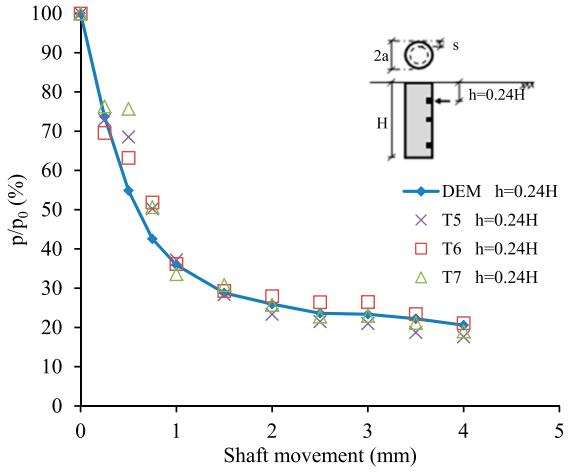

Fig. 12. Normalized pressures on the shaft at a depth of 0.24*H*

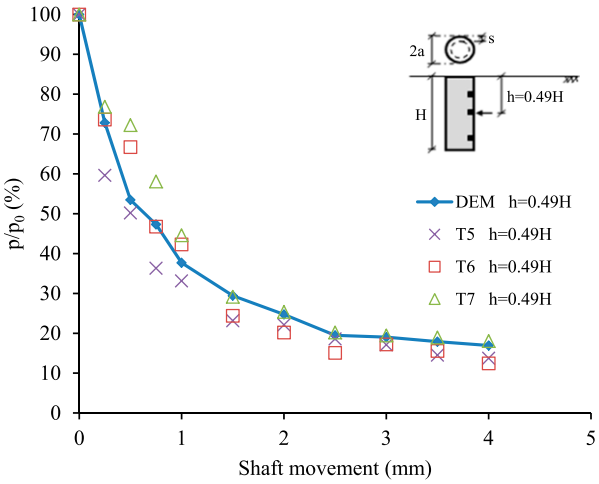

Fig. 13. Normalized pressures on the shaft at a depth of 0.49*H*

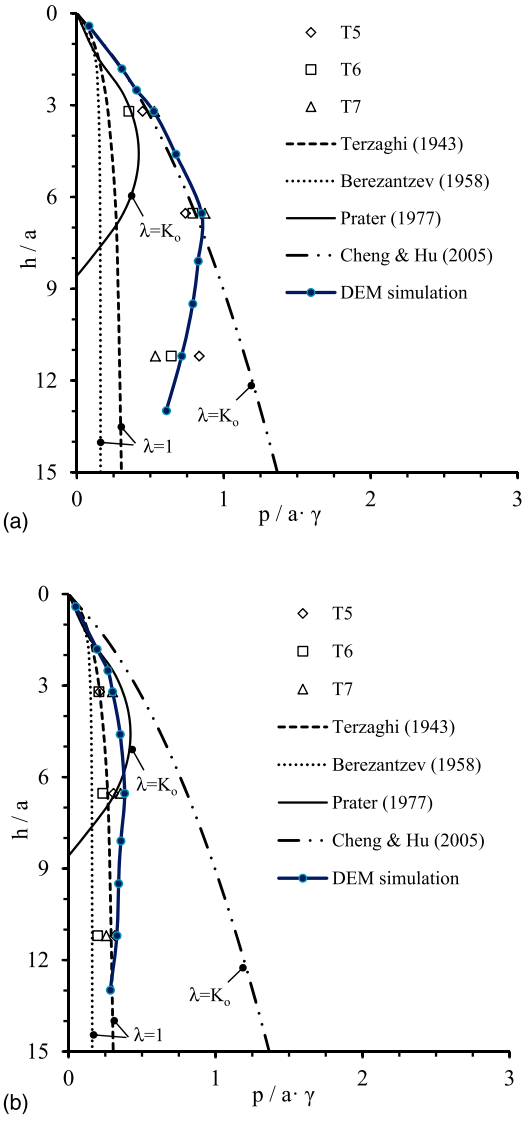

Fig. 15. Comparison between modeled results and theoretical earth pressures along the shaft: (a) shaft movement = 1 mm; (b) shaft movement = 4 mm

Int. J. Geomech. 2014.14:80-91.

For the same wall movement, the measured earth pressures reached approximately 65% at 0.24 and 0.49H and approximately 50% at 0.84H. With a further increase in wall movement, the DEM results were found to be identical to the measured values. For movement between 1 and 2 mm, the earth pressure decreased to 25% of the initial value at 0.24 and 0.49H and to 18% at 0.84H. Further wall movement (greater than 3 mm) did not cause a significant pressure reduction, and the lateral pressures became constant when they reached approximately 20% of the initial value at 0.24 and 0.49H and approximately 10% at 0.84H. It can be concluded that the axisymmetric active earth pressure fully develops when the shaft wall moves approximately 2–3 mm or approximately 2.5–4% of the shaft radius. Furthermore, the most rapid reduction in the earth pressure is observed near the bottom of the shaft.

Earth Pressure Distribution with Depth

Fig. 15 shows the calculated and measured earth pressure distributions with depth. Earth pressure values are normalized with respect to the shaft radius and soil unit weight while the depth is normalized with respect to the shaft radius. For a wall movement of 1 mm or 0.1% of the shaft height, both the calculated and measured earth pressures showed an increase from the sand surface to the middle of the shaft with a gradual decrease toward the shaft base. The earth pressure continued to decrease with the increase in wall movement up to 4 mm or 0.4% of the shaft height. It can be seen that at this wall movement, the pressure distribution became more uniform with depth. The preceding results are compared with different analytical solutions, including the methods of Terzaghi (1943), Berezantzev (1958), Prater (1977), and Cheng and Hu (2005).

It is realized that the pressure distributions following the solutions of Terzaghi and Berezantzev with the earth pressure coefficient on radial planes, λ, equal to 1 are in good agreement with the numerical and experimental results, provided that enough wall movement is allowed. These two solutions suggest a quite uniform pressure distribution with depth. Prater's solution, which is based on Coulomb's wedge analysis with the value $\lambda = K_o$, leads to 0 earth pressure at h/a of approximately 9. This is inconsistent with the numerical and experimental results. However, the solution suggested that the maximum earth pressure can be used for design purposes. In the case of small wall movement, the upper bound solution with $\lambda = K_o$, as proposed by Cheng and Hu, provides a good agreement with the calculated and measured values for the upper half of the shaft. However, the method indicates a continuing increase in the lateral pressure with depth, which is not consistent with the experimental results. The preceding comparisons suggest that there is a strong relationship between lateral earth pressure and soil movement around the shaft.

Extent of Shear Failure

Fig. 16 shows the displacement field around the shaft for a wall movement of 3 mm. It can be seen that a nonuniform failure zone of conical shape has developed along the shaft, as illustrated in Fig. 16(b). The zone increased in size from the bottom of the shaft up to a region of 0.2 m in radius at the surface (approximately 2.5 times the shaft radius). The angle α that the failure surface makes with the horizontal is found to be approximately 75°. This observed failure region is consistent with the stress distributions discussed in the previous sections.

Fig. 17 shows a cross-sectional view of the contact force network within the DEM domain for the cases of no wall movement (initial state) and a wall movement of 3 mm. Each contact force is illustrated by a line connecting the centers of two contacting particles, while the

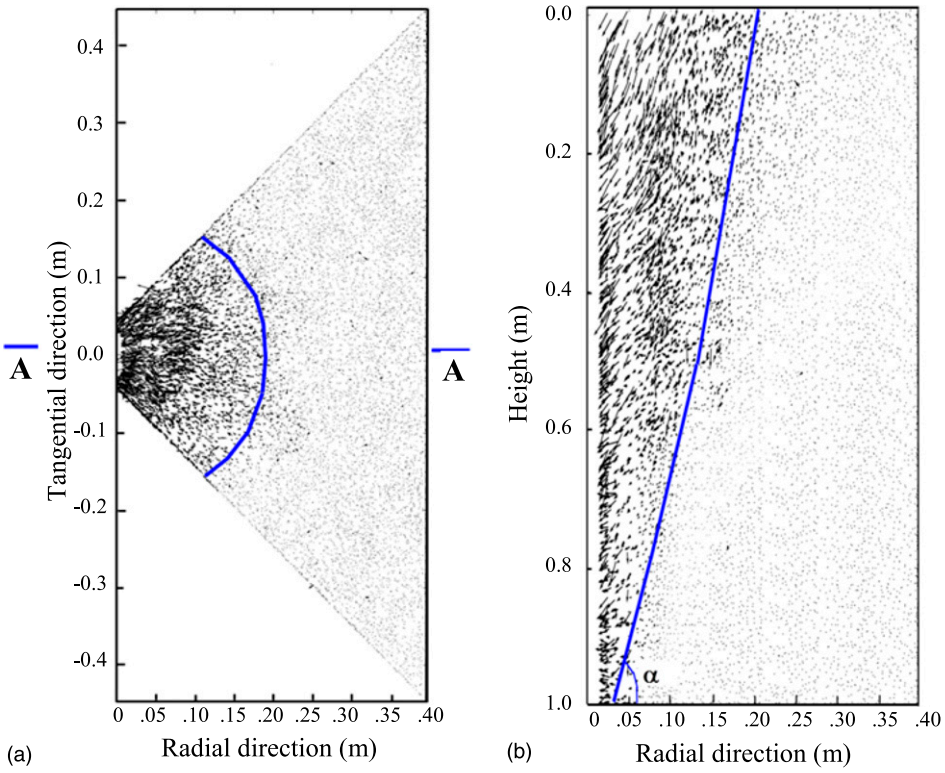

Fig. 16. Displacement field at shaft movement of 3 mm: (a) plan view; (b) cross-sectional A-A view

Int. J. Geomech. 2014.14:80-91.

width of the line is proportional to the magnitude of the normal contact force. It can be observed that when the shaft radius is reduced, the contact forces within the shear failure zone decreased in the radial direction and increased in the circumferential direction.

Stress Distribution within the Soil

Stresses within the soil mass, including the radial, circumferential, and vertical components (see Fig. 18), are analyzed at a chosen depth of 0.49*H* using the DEM. Fig. 19 shows the radial stress versus radial distance from the shaft center. It can be seen in Fig. 19(a) that radial stresses near the shaft wall dropped rapidly when the wall moved 1 mm. An increase in wall movements from 2 to 3 mm caused the radial stress to further decrease. However, no significant change in radial stress was observed for movements larger than 3 mm. The radial stress in the vicinity of the shaft remained at approximately 60% of the initial value for a wall movement of 1 mm and approximately 40% for a wall movement of 3 mm. Fig. 19(b) shows the distribution of the radial stresses in a selected cross section. It was found that the changes in radial stresses mostly occurred within a distance of 0.3 m from the center of the shaft. The stresses outside this region remained close to its initial values despite the induced wall movement.

It is noted that the relief of radial stresses due to soil movement caused vertical (along the shaft height) and horizontal (in the circumferential direction) arching, and resulted in stress redistribution in the vicinity of the shaft. Fig. 20 shows the circumferential stresses versus the radial distance. It can be seen that the circumferential stresses near the shaft were smaller than the initial values for all induced wall movements. At a distance of approximately 0.2 m from the shaft center, circumferential stresses reached a maximum value and decreased with distance to approach the initial state far away from the shaft. It can also be seen from Fig. 20(a) that larger wall movements lead to slightly larger circumferential stresses. The largest circumferential stress was reached at a wall displacement of 4 mm and was found to be approximately 10% higher than the initial circumferential stress. Fig. 20(b) shows a contour plot of the circumferential stress distribution around the shaft. It can be seen from the figure that for a shaft movement larger than 3 mm, no significant changes to the stress distribution occurred. This confirms that soil failure has already been established at a wall movement of approximately 2–3 mm. At that stage, the gravity effect dominates, leading to the development of a stable arch with nearly constant circumferential and radial stresses.

Fig. 21 shows the calculated stress components near the middle of the wall when the wall movement reached 2 mm. The circumferential stresses were found to be slightly larger than the radial stress in the close vicinity of the shaft. However, at a distance of 0.3 m from the shaft wall, the circumferential and radial stress components converged and became equal to the stresses corresponding to the rest condition.

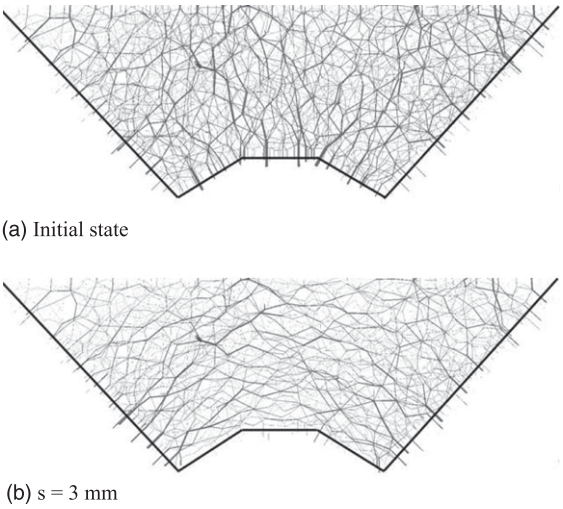

Fig. 17. Contact force networks: (a) initial state; (b) at a shaft movement of 3 mm

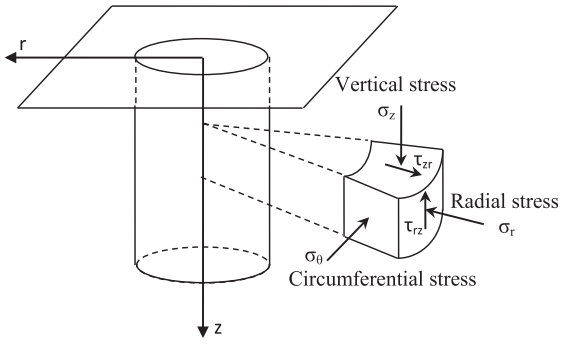

Fig. 18. Stresses acting on a soil element

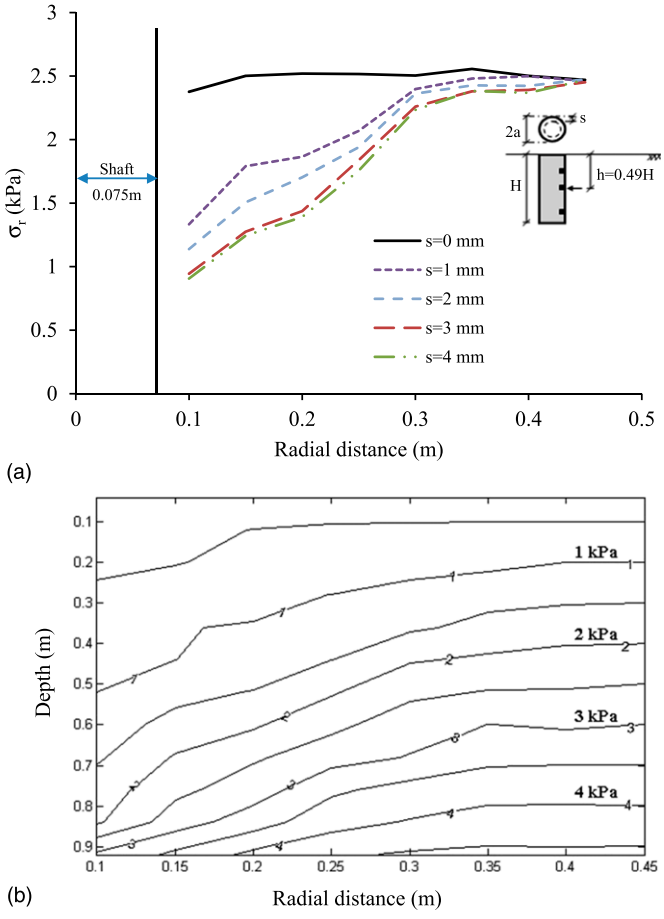

Fig. 19. Radial stress distribution: (a) at a depth of 0.49*H*; (b) in the cross section A-A ($s = 3$ mm)

Int. J. Geomech. 2014.14:80-91.

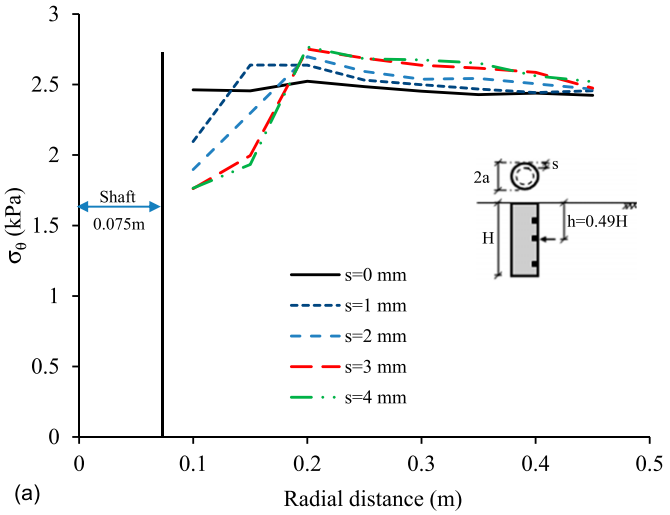

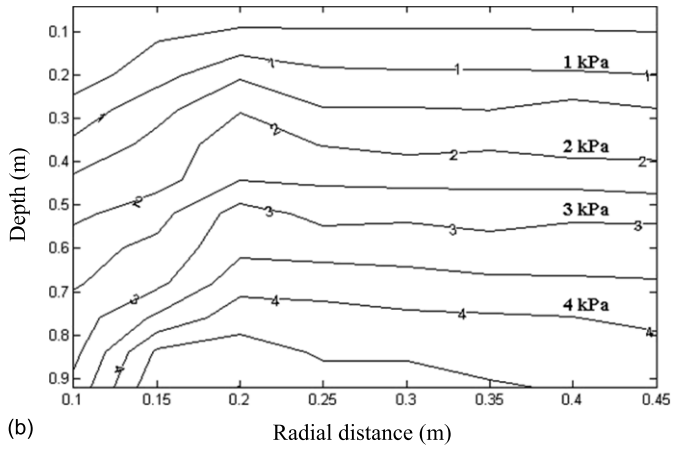

Fig. 20. Circumferential stress distribution: (a) at a depth of 0.49H; (b) in the cross section A-A (s = 3 mm)

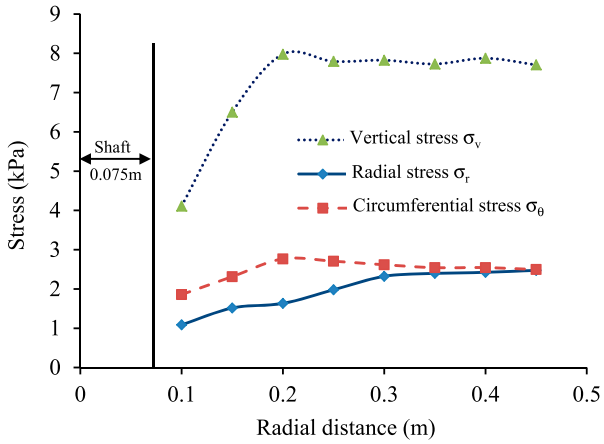

Fig. 21. Stress components at a depth of 0.49H and shaft movement of 2 mm

Summary and Conclusions

In this paper, an experimental study was performed to investigate the lateral earth pressure acting on a cylindrical shaft. The axisymmetric geometry of the test setup allowed for a proper measurement of the lateral earth pressure. A numerical investigation was then performed using a specifically designed DEM model. A modified multilayer gravitational packing method that is able to capture some of the important properties was proposed to generate the soil domain. The particle size distribution of the sand used in the experiments was considered, and a calibration was conducted using direct shear test results to determine the input parameters needed for the discrete element analysis. A quarter of the shaft geometry was numerically modeled, and the lateral pressures acting on the shaft wall were recorded. Stresses within the soil domain were calculated, and the arching effect was discussed. The results of the experimental and numerical studies were also compared against some of the available analytical solutions.

The results of the DEM analysis of the vertical shaft agreed well with the experimental data. Based on the physical and numerical studies, a small shaft movement can lead to a rapid decrease in the earth pressure acting on the shaft wall. The required shaft movement to reach the full active condition was found to range from 2.5 to 4% of the shaft radius or 0.2 to 0.3% of the shaft height. At this wall movement, the earth pressure can significantly decrease to a value of 10% of the initial value and the lateral pressure becomes uniform with depth. The analytical solutions of Terzaghi and Berezantzev were found to be in good agreement with the observed pressure distribution.

The movement of the shaft wall resulted in a redistribution of stresses within the soil medium. The arching effect has lead to a decrease in radial stresses and an increase in circumferential stresses within a region defined by a radius 0.3 m from the shaft center. The stresses in the soil domain became quite stable when the wall movement reached 3 mm. The agreement between the numerical and measured results demonstrated the efficiency of the DEM in validating geotechnical problems involving granular material and large deformations.

Acknowledgments

This research is supported by a research grant from the Natural Sciences and Engineering Research Council of Canada (NSERC). The financial support provided by the McGill Engineering Doctoral Award (MEDA) to the first author is greatly appreciated. The authors also wish to acknowledge Tatiana Tobar for the experimental work done at McGill University.

References

Andresen, L., Jostad, H. P., and Andersen, K. H. (2011). "Finite element analyses applied in design of foundations and anchors for offshore structures." *Int. J. Geomech.*, 10.1061/(ASCE)GM.1943-5622.0000020, 417–430.

Belheine, N., Plassiard, J.-P., Donzé, F.-V., Darve, F., and Seridi, A. (2009). "Numerical simulation of drained triaxial test using 3D discrete element modeling." *Comput. Geotech.*, 36(1–2), 320–331.

Berezantzev, V. G. (1958). "Earth pressure on the cylindrical retaining walls." *Conf. on Earth Pressure Problems,* International Society of Soil Mechanics and Foundation Engineering, Belgian Group, Brussels, Belgium, 21–27.

Calvetti, F. (2008). "Discrete modelling of granular materials and geotechnical problems." *Eur. J. Environ. Civ. Eng.*, 12(7–8), 951–965.

Chen, C., McDowell, G. R., and Thom, N. H. (2012). "Discrete element modelling of cyclic loads of geogrid-reinforced ballast under confined and unconfined conditions." *Geotextile Geomembr.*, 35, 76–86.

Int. J. Geomech. 2014.14:80-91.

Cheng, Y. M., and Hu, Y. Y. (2005). "Active earth pressure on circular shaft lining obtained by simplified slip line solution with general tangential stress coefficient." *Chin. J. Geotech. Eng.*, 27(1), 110–115.
Cheng, Y. M., Hu, Y. Y., and Wei, W. B. (2007). "General axisymmetric active earth pressure by method of characteristics—Theory and numerical formulation." *Int. J. Geomech.*, 10.1061/(ASCE)1532-3641(2007)7:1(1), 1–15.
Cheung, G. (2010). "Micromechanics of sand production in oil wells." Ph.D. thesis, Imperial College London, London.
Chun, B., and Shin, Y. (2006). "Active earth pressure acting on the cylindrical retaining wall of a shaft." *South Korea Ground Environ. Eng. Journal*, 7(4), 15–24.
Cui, L., and O'Sullivan, C. (2006). "Exploring the macro- and micro-scale response of an idealised granular material in the direct shear apparatus." *Géotechnique*, 56(7), 455–468.
Cundall, P. A., and Strack, O. D. L. (1979). "A discrete numerical model for granular assemblies." *Géotechnique*, 29(1), 47–65.
Herten, M., and Pulsfort, M. (1999). "Determination of spatial earth pressure on circular shaft constructions." *Granular Matter*, 2(1), 1–7.
Itasca. (2004). *PFC 2D 3.10 particle flow code in two dimensions, theory and background volume*, 3rd Ed., Minneapolis.
Jenck, O., Dias, D., and Kastner, R. (2009). "Discrete element modelling of a granular platform supported by piles in soft soil – Validation on a small scale model test and comparison to a numerical analysis in a continuum." *Comput. Geotech.*, 36(6), 917–927.
Jiang, M. J., Konrad, J. M., and Leroueil, S. (2003). "An efficient technique for generating homogeneous specimens for DEM studies." *Comput. Geotech.*, 30(7), 579–597.
Konig, D., Guettler, U., and Jessberger, H. L. (1991). "Stress redistribution during tunnel and shaft construction." *Proc., Int. Conf. Centrifuge 1991*, H.-Y. Ko and F. G. McLean, eds., Balkema, Rotterdam, Netherlands, 129–135.
Kozicki, J., and Donze, V. F. (2009). "YADE-OPEN DEM: An open-source software using a discrete element method to simulate granular material." *Eng. Computat.*, 26(7), 786–805.
Labra, C., and Oñate, E. (2009). "High density sphere packing for discrete element method simulations." *Commun. Numer. Methods Eng.*, 25(7), 837–849.
Ladd, R. S. (1978). "Preparing test specimens using undercompaction." *Geotech. Test. J.*, 1(1), 16–23.
Lade, P. V., Jessberger, H. L., Makowski, E., and Jordan, P. (1981). "Modeling of deep shafts in centrifuge test." *Proc., Int. Conf. on Soil Mechanics and Foundation Engineering*, Vol. 1, Balkema, Rotterdam, Netherlands, 683–691.
Liu, S. H., Sun, D., and Matsuoka, H. (2005). "On the interface friction in direct shear test." *Comput. Geotech.*, 32(5), 317–325.
O'Sullivan, C. (2011). *Particulate discrete element modeling, a geomechanics perspective*, Spon Press/Taylor & Francis, London and New York.
O'Sullivan, C., and Cui, L. (2009). "Micromechanics of granular material response during load reversals: Combined DEM and experimental study." *Powder Technol.*, 193(3), 289–302.
Osman, A. S., and Randolph, M. F. (2012). "Analytical solution for the consolidation around a laterally loaded pile." *Int. J. Geomech.*, 10.1061/(ASCE)GM.1943-5622.0000123, 199–208.
Potyondy, D. O., and Cundall, P. A. (2004). "A bonded-particle model for rock." *Int. J. Rock Mech. Min. Sci.*, 41(8), 1329–1364.
Prater, E. G. (1977). "Examination of some theories of earth pressure on shaft linings." *Can. Geotech. J.*, 14(1), 91–106.
Salgado, R., and Prezzi, M. (2007). "Computation of cavity expansion pressure and penetration resistance in sands." *Int. J. Geomech.*, 10.1061/(ASCE)1532-3641(2007)7:4(251), 251–265.
Šmilauer, V., et al. (2010). "Yade documentation." *The Yade project 2010*, ⟨http://yade-dem.org/doc/⟩ (Oct. 28, 2013).
Terzaghi, K. (1943). *Theoretical soil mechanics*, Wiley, New York.
Thornton, C., and Zhang, L. (2003). "Numerical simulations of the direct shear test." *Chem. Eng. Technol.*, 26(2), 153–156.
Tobar, T. (2009). "An experimental study of the earth pressure distribution on cylindrical shafts." M.S. thesis, McGill Univ., Montréal.
Tobar, T., and Meguid, M. A. (2011). "Experimental study of the earth pressure distribution on cylindrical shafts." *J. Geotech. Geoenviron. Eng.*, 10.1061/(ASCE)GT.1943-5606.0000535, 1121–1125.
Walz, B. (1973). "Left bracket apparatus for measuring the three-dimensional active soil pressure on a round model caisson right bracket." *Baumaschine und Bautechnik*, 20(9), 339–344 (in German).
Weatherley, D., Boros, V., and Hancock, W. (2011). *ESyS – Particle tutorial and user's guide version 2.1*, Univ. of Queensland, Brisbane, Australia.
Yan, Y., and Ji, S. (2010). "Discrete element modeling of direct shear tests for a granular material." *Int. J. Numer. Anal. Methods Geomech.*, 34(9), 978–990.